



High on-chip gain spiral $\text{Al}_2\text{O}_3:\text{Er}^{3+}$ waveguide amplifiers

D. B. BONNEVILLE,^{†,*} C. E. OSORNIO-MARTINEZ,[†]  M. DIJKSTRA,
AND S. M. GARCÍA-BLANCO 

Integrated Optical Systems, MESA+ Institute for Nanotechnology, University of Twente, 7500 AE Enschede, The Netherlands

[†]These authors both contributed equally to this work

*d.b.bonneville@utwente.nl

Abstract: We demonstrate reactively sputtered $\text{Al}_2\text{O}_3:\text{Er}^{3+}$ waveguide amplifiers with an erbium concentration of 3.9×10^{20} ions/cm³, capable of achieving over 30 dB small signal net gain at 1532 nm using bidirectional pumping at 1480 nm. We observe on chip output powers of 10.2-13.6 dBm of amplified signal power at 1532 nm for a 12.9 cm waveguide amplifier considering -25.4 dB of lumped coupling losses per facet. Annealing was used to improve the performance of the devices, which were patterned using electron beam lithography and reactive ion etching. This result, to our knowledge, represents record breaking on-chip internal net gain for $\text{Al}_2\text{O}_3:\text{Er}^{3+}$ waveguide amplifiers, which show promise over other technologies due to wafer scalability and promise of easy monolithic integration with other material platforms to support a wide variety of applications.

© 2024 Optica Publishing Group under the terms of the [Optica Open Access Publishing Agreement](#)

1. Introduction

Rare earth ion doped media in photonic integrated circuits (PICs) is emerging as a competitive optical amplification platform for a wide variety of applications, ranging from telecommunications [1], light detection and ranging (LIDAR) [2] and datacoms to environmental and biological sensing [3,4] and metrology [5]. The necessity and drive of many industries and applications to decrease size, cost and performance of optical components is causing a paradigm shift in optical amplifiers and lasers as they move towards planarized integrated photonic platforms. These platforms consist of a variety of materials such as Ta_2O_5 [6], TeO_2 [7–9], Al_2O_3 [10–12], LiNbO_3 [13,14], and Si_3N_4 [15], with rare earth dopants such as Yb^{3+} [4], Er^{3+} [1,2,4,7,9,10–13,15,16], Tm^{3+} [9,17], $\text{Er}^{3+}:\text{Yb}^{3+}$ [14,18], and Nd^{3+} [19] to cover a variety of wavelengths for different applications. Compared to semiconductor optical amplifiers (SOAs), which are electrically pumped and have very high gain per unit centimeter [20], rare earth doped amplifiers are optically pumped and are typically several centimeters long. On the other hand, SOAs are typically integrated with techniques such as wafer bonding [21], micro-transfer printing [22] or butt-coupling [23], which increases the complexity and cost of the fabrication process, which also relies on epitaxy to form the gain material. The benefits from rare earth ion doped materials are becoming evident for many applications that require high signal powers that do not suffer from inhomogeneous broadening, exhibit very low-noise figures and show temperature stable operation. Such applications include LIDAR, spectroscopy and environmental sensing in harsh environments. It is therefore clear that there is a necessity for a scalable platform, compatible with VLSI CMOS processing, to realize optical amplifiers and lasers that can be easily integrated with other platforms and devices.

To realize such a platform many techniques have been demonstrated consisting mainly of atomic layer deposition (ALD) [24] and reactive magnetron sputtering [25]. It has also been recently demonstrated that Si_3N_4 doped with Er^{3+} through ion-implantation can compare and, in some cases, outcompete commercial erbium doped fiber amplifiers (EDFAs) and SOAs in terms

of net output powers [15] for the telecommunication market [26]. However, both ion implantation of Er^{3+} and ALD deposition of doped materials is not a manufacturable approach, although some efforts have been directed towards the establishment of many wafers ALD instruments to increase its scaling potential [27]. Reactive magnetron sputtering allows for relatively fast wafer level deposition, in-situ doping of the host material with solid purity-controlled targets and does not require dopant activation with high temperature annealing (above 1000°C [15]). Al_2O_3 is a promising candidate host for rare earth ion dopants due to its high rare earth ion solubility allowing high ion concentration, low passive background losses from 1–5 dB/m [25], and broadband transparency permitting low-loss operation from blue and UV wavelengths [28] all the way to the near infrared [5]. It has also been demonstrated as a compatible process with other mature passive waveguide platforms such as Si_3N_4 for multi-layer monolithic integration of passive-active components [1,5,17,29–31] with well-known spectroscopy for its amorphous state [32].

Recent advances towards deposition of high-index polycrystalline Al_2O_3 [33] have demonstrated high on-chip output laser powers above 1 W for Tm^{3+} doped devices [5], femtosecond pulse amplification (i.e., 116 fs) with peak power of 800 W [17,30] as well as on-chip powers up to 28 mW in Er^{3+} doped amplifiers integrated monolithically with Si_3N_4 [34].

In this work we demonstrate reactively sputtered polycrystalline $\text{Al}_2\text{O}_3:\text{Er}^{3+}$ waveguides formed through electron beam lithography and reactive ion-etching to realize optical amplifiers with high on-chip gain. Using 1480 nm pumping, an internal on-chip gain of 33.3 dB is obtained at 1532 nm, resulting in an on-chip power of ~ 10 mW. To our knowledge this represents the highest reported on-chip gain for $\text{Al}_2\text{O}_3:\text{Er}^{3+}$ amplifiers. Devices demonstrated high coupling losses and consequentially amplifier lengths are limited to < 13 cm. However, moving forward, optimization of the edge couplers, cross section and length of the amplifiers points towards promising pathways of improving the results presented here.

2. Fabrication

Film deposition was performed in the MESA + Nanolab clean-room facilities using reactive magnetron sputtering (AJA ATC 1500) following procedures outlined in [35]. A silicon wafer (10 cm in diameter) with an 8 μm thick thermal oxide layer was used as a substrate and loaded to a rotating holder at a distance of 15.2 cm from the magnetrons. A turbomolecular pump was used to pre-evacuate the deposition chamber to a base pressure of 40 μPa . Two magnetrons designed for 2-in targets were used for the deposition, each one with its independent RF power source. Sputtering powers of 200 W and 18 W were applied to the aluminum (Al, 99.9995% purity) and erbium (Er, 99.95% purity) targets, respectively. Gas flows of 30 sccm of argon and 2.8 sccm O_2 were utilized. The temperature of the holder was set 760°C (expected wafer temperature of $\sim 610^\circ\text{C}$ based on [35]) and a process pressure of 0.53 Pa.

The resulting $\text{Al}_2\text{O}_3:\text{Er}^{3+}$ layer had a thickness of 786 nm (i.e., deposition rate of 3.74 nm/min) with a refractive index of 1.739 at 1030 nm, which was measured using variable angle spectroscopic ellipsometry (VASE). Erbium concentration of the layer is approximately known to be 3.9×10^{20} ions/ cm^3 using calibrated sputtering powers based on Rutherford backscattering measurements (RBS) [36]. Samples were stored in N_2 ambient in between fabrication steps to avoid OH^- contamination, which is a known source of recombination centers in erbium doped amplifiers [37]. Electron-beam lithography (EBL) was used to pattern negative resist at a dose of $1000 \mu\text{C}/\text{cm}^2$ to be used as an etch mask for the definition of spirals, ring resonators and straight waveguides for signal enhancement and background loss characterization. Reactive ion-etching (RIE) was performed to define the waveguides. Plasma-enhanced chemical vapor deposition (PECVD) was used to deposit a SiO_2 cladding at a deposition rate of 37 nm/min using 200 and 710 sccm of SiH_4/N_2 and N_2O respectively, with a chamber pressure of 650 mTorr at 300°C stage temperature and 60 W of power. Chips were diced and annealed at 550°C in a tube furnace

with N_2 ambient. In order to reduce the coupling losses (α_c) and demonstrate the compatibility of the process, chip facet polishing was performed using a FLE x Waveguide Polisher from KrellTech with a variety of polishing pads of varying roughness of 3.0, 1.0 and 0.3 μm wet with demi water.

3. Design and characterization

Figure 1(a) shows the designed cross section of the waveguide amplifier, which was optimized for high overlap with the gain material (i.e., 79% at 1532 nm). Multimode operation exists at the dimensions shown in Fig. 1(a) but are rejected by single mode spot size converters at the input and output facets of the chip. Nanotapers with a tip width of 150 nm and a length of 2 mm were designed for coupling to and from the chip in order to maximize the overlap between the facets and a wavelength dependent fiber mode field diameter (MFD), which is $10.0 \pm 0.4 \mu\text{m}$ at 1532 nm. The fabricated width of 303 nm is overlaid (i.e., green vertical line) demonstrating the simulated coupling losses at the actual widths as measured via scanning electron microscopy (SEM) shown in Fig. 1(b). Artifacts from the morphology of the nonconformal plasma enhanced chemical vapor deposition (PECVD) process used to deposit the SiO_2 cladding can be seen in Fig. 1(b), which are anticipated to have contributed to additional coupling and background propagation losses. The simulated losses calculated from the overlap for a variety of taper widths is shown in

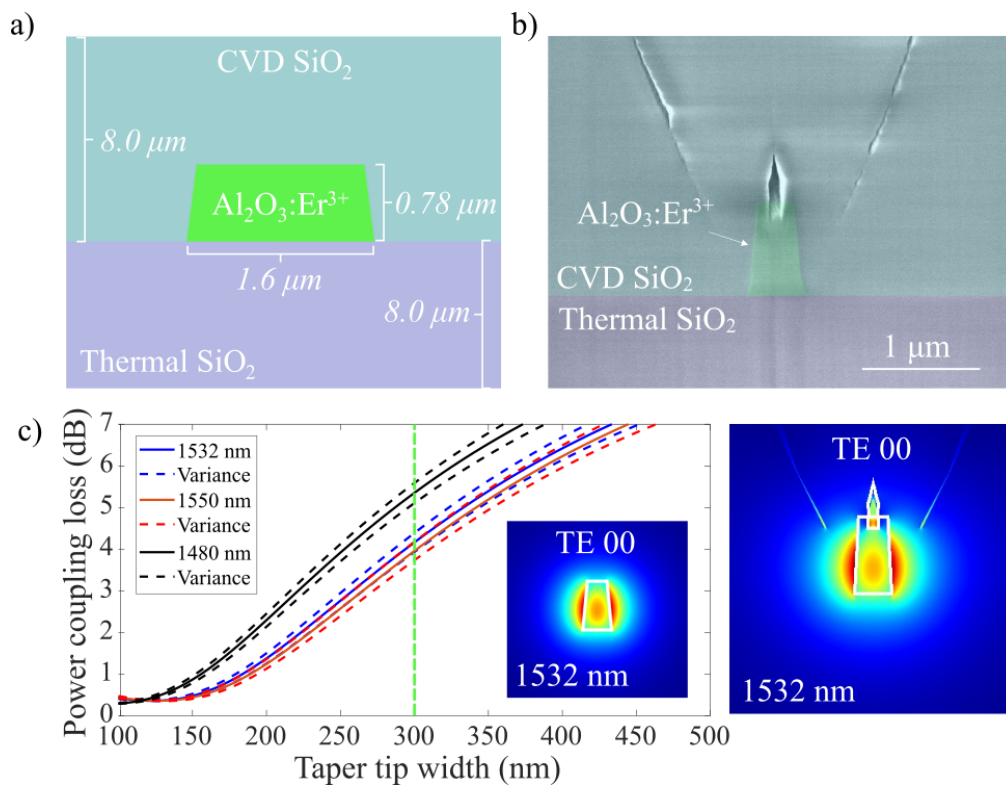


Fig. 1. a) 2D cross section of the waveguide design with overlaid dimensions. b) SEM of the cross section of a taper used for expanding the mode and coupling to fiber. c) Coupling loss as a function of taper tip width for the fundamental TE mode shown in the inset at 1532 nm with a green dashed line overlaid on the measured width of 303 nm (left), as well as a mode simulation which includes the voids seen in the facet of the reported nanotapers (right).

Fig. 1(c) for pump and signal wavelengths, as well as an inset of the mode at the facet. Alongside Fig. 1(c) is a mode simulation which includes the voids shown in the fabricated nanotapers.

4. Experimental results

Waveguide absorption losses due to erbium dopants were measured using an InGaAs IR camera (Xenics Bobcat 320) to collect the light normally scattered from the sample [12,29]. Background losses were verified by means of ring resonator measurements at ~ 1635 nm, which is outside of the erbium absorption band. Polarization maintaining (PM) fibers and a tunable laser were used to couple light to $\text{Al}_2\text{O}_3:\text{Er}^{3+}$ spirals of varying length and a ring resonator with a radius of $300\ \mu\text{m}$ and a coupling gap of $1.4\ \mu\text{m}$. Figure 2(a) shows a sample set of intensity measurements taken from regions of interest across the spiral, which are fit to exponentials that follow the Beer-Lambert law [12] to extract the losses in dB/cm at 1532, 1550 and 1640 nm. The insets show the images used for processing at each wavelength. This was performed for a variety of signal powers shown in Fig. 2(b) to ensure that ground state population dependent absorption was not affecting the losses being used for the gain calculations. To ensure an accurate estimation of the absorption losses, the signal power was kept in the small signal regime as discussed in [29] as absorption losses are known to decrease for higher launched powers due to depopulation of the Er ions ground state. Total waveguide losses of 2.3 and 1.7 ± 0.2 dB/cm are used for gain calculations at 1532 and 1550 nm respectively, taken from a statistical observation of the data taken in the small signal regime (~ 30 dBm launched signal). An error on the losses was assigned according to the variation in the fitting and R^2 values shown in Fig. 2(a). These values from the IR camera measurements represent the total waveguide loss, including absorption from the erbium and background propagation losses, and are not impacted by the coupling losses. In order to more accurately measure the background losses, a ring resonator was used in which a critically coupled ring was fit with a Lorentzian line shape to extract the waveguide losses at ~ 1635 nm. Figure 2(c) shows the transmission of the bus waveguide with coupled ring resonances from 1470–1640 nm. A finer resolution scan is shown in Fig. 2(d) with the overlapped fit that was used to extract a background propagation loss of 0.46 dB/cm. To ascertain the launched signal power on the chip, from the incident signal power measured before the chip, a measurement was performed in which the system losses and measured waveguide losses were accounted for. This resulted in very high values and was also shown to depend on the signal wavelength and power. This is anticipated to be exacerbated by the air void seen in Fig. 1(c), and the additional scattering and losses due to the overlap with the feature and the voids inner sidewalls which appear rough. Mode simulations including the void demonstrate an overlap of $\sim 11\%$ which contributes substantial losses. Additionally, the wavelength and power dependence seems to indicate that the erbium absorption is variable for the nanotaper region of the chip, likely due to the difference in overlap and mode evolution over the $2000\ \mu\text{m}$ of interaction length. These two loss mechanisms for ease are referred to lumped coupling losses here, to represent the void, and the nanotaper mode mismatch as well as absorption along its length.

Bidirectional pumping was then utilized at 1480 nm using butterfly mounted pump diodes, which were coupled to the chip using external wavelength division multiplexers (WDMs). Pump powers shown are therefore the addition of both pumps, and this was required to fully excite the spiral amplifier along its length. A tunable C-band laser and two separate diode lasers were used to launch low and high signal powers respectively at 1532 and 1550 nm. The signal was measured using an optical spectrum analyzer (OSA) after passing through a low-pass filter to block signals below 1500 nm to get a more accurate assessment of the power and to better filter the 1480 nm pump. This setup is shown in Fig. 3(a). PM fiber was used throughout the setup with angled fiber connections before the chip and flat facets to couple to the chip in order to avoid additional fluctuations from Fabry Perot resonances, which can lead to parasitic lasing when in

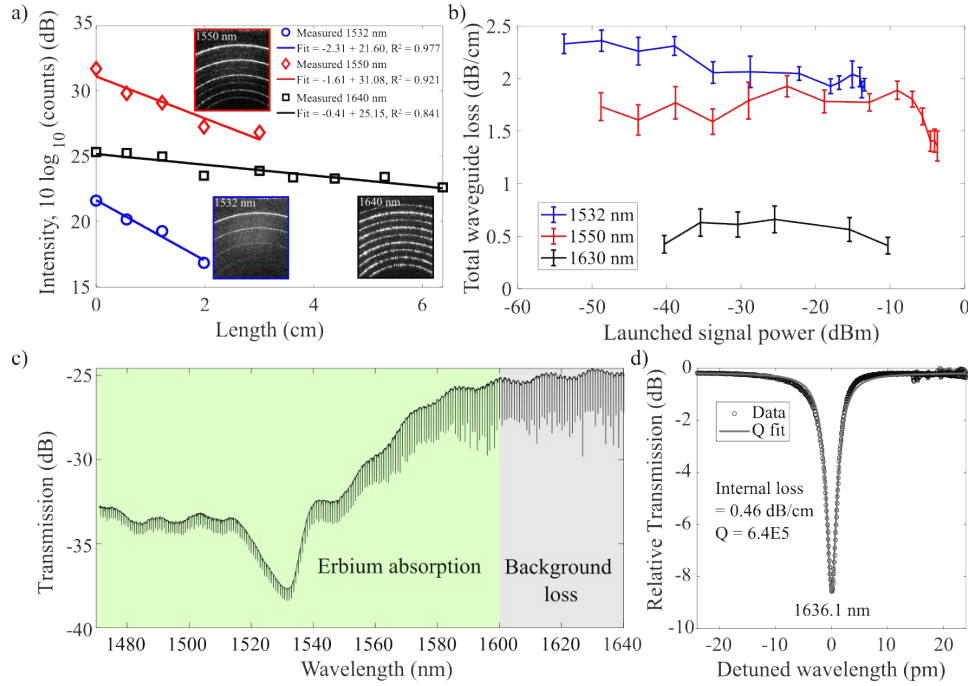


Fig. 2. a) Intensity of scattered light collected normally out the chip using an IR camera along with the linear fits corresponding to the losses for 1532, 1550 and 1630 nm. Insets show the raw images used to fit data vs. the waveguide length of the spiral. b) Waveguide losses for 1532, 1550 and 1630 nm taken from IR camera measurements for a variety of signal powers. c) Transmission from a ring used for background waveguide loss measurements showing the regime where erbium absorption is negligible beyond 1600 nm. d) A high-resolution scan of a ring resonance spectra used for calculating the background losses using a Lorentzian fit for the internal quality factor.

very high gain regimes (+ 26 dB in [15]). Polarization control was not utilized as the nanotapers reject TM modes, which could potentially be excited over the length of the amplifier. Piezo controlled stages were utilized to optimize the coupling to and from the chip. Figure 3(b) shows a typical set of measurements of OSA spectra for varying pump powers at a given incident signal power (-4.8 dBm) and wavelength (1531.5 nm). Here important values are obtained, which are used to calculate the gain via the signal enhancement (SE) method. The SE is calculated using the difference between the measured signal with the pump on (T_{on}), versus the signal with the pump off (T_{off}). The SE is then calculated by subtracting the additional power contribution from the amplified spontaneous emission (ASE), which must remain at least 5 dB below the measured gain signal (T_{on}). Finally, the erbium absorption (α_{abs}) and background waveguide losses (α_{BG}) are removed in order to calculate the on-chip (internal) net gain of the waveguide amplifier.

$$Internal\ Net\ Gain\ [dB] = 10 * \log\left(\frac{T_{on}(mW) - ASE(mW)}{T_{off}(mW)}\right) - \alpha_{abs} - \alpha_{BG}$$

Figure 3(c) shows the on-chip internal net gain using this method. Various regimes are shown in different colors to represent the different loss regimes of the amplifier. Over 30 dB of on-chip net gain is observed at peak pump powers.

In order to assess gain at higher signal powers to observe saturation of the signal enhancement, the power at 1532 and 1550 nm was varied across the small and high signal power regimes at a

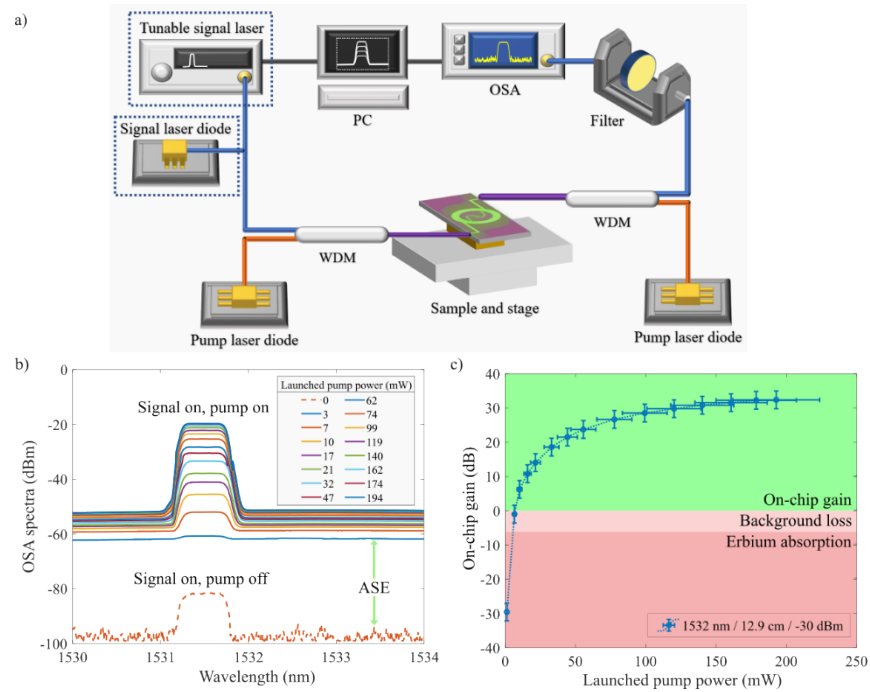


Fig. 3. Setup used for measuring the gain in fabricated amplifiers with bidirectional pumping using off-chip WDMs and a filter to cut-off spectra below 1500 nm. Two signal sources are used for switching from low to high power signal regimes. b) OSA spectra from a measurement of varying pump power for a launched signal of -29.8 dBm and a 12.9 cm spiral length. c) On-chip net gain as a function of increasing pump power. Overlaid regions of colour represent the evolution from loss to on-chip gain.

fixed pump power utilizing different signal sources to access each power regime. Figure 4(a) shows a sample OSA spectra for a 12.9 cm spiral amplifier with ~63 dB SE. Figure 4(b)–(c) shows SE, on-chip net gain, and on-chip signal power respectively for varying waveguide lengths. Peak small signal gain per unit centimeter of 3.5 dB/cm is shown for a 4.9 cm long waveguide at 1532 nm. Peak net internal gain values of 33.5 ± 1.3 dB are observed for a launched signal power of -30.2 dBm (i.e., small signal) in a 12.9 cm long spiral amplifier. The uncertainties quoted are derived from the variation in waveguide losses as well as an averaging of three OSA spectra per data point to ensure stable power measurements. The contribution from variation in power over time of repeated measurements is negligible compared to the error in waveguide losses, which explains the smaller error in the SE measurements.

System measurements were carried out to understand the loss contribution of the different sections of the system. The power incident on the chip (P_{inc}), the power measured at the OSA (P_{OSA}), the total loss of the system (α_{sys}) and the loss of the OSA (α_{OSA}) were individually characterized. P_{inc} was measured by connecting the input fiber to a photodetector. P_{OSA} is the power measured at the OSA, consisting of the power output of the chip after passing through the WDM that separates pump and signal. α_{sys} takes into account the fiber, WDM and connection to the OSA losses. Finally, the α_{OSA} , represents the loss at the input of the OSA, measured as the difference of powers between the photodetector and the OSA. Considering this analysis, the coupling losses to the PIC can be estimated as:

$$\alpha_c = 0.5 * (P_{OSA} - P_{inc} - \alpha_{sys} - gain - \alpha_{OSA})$$

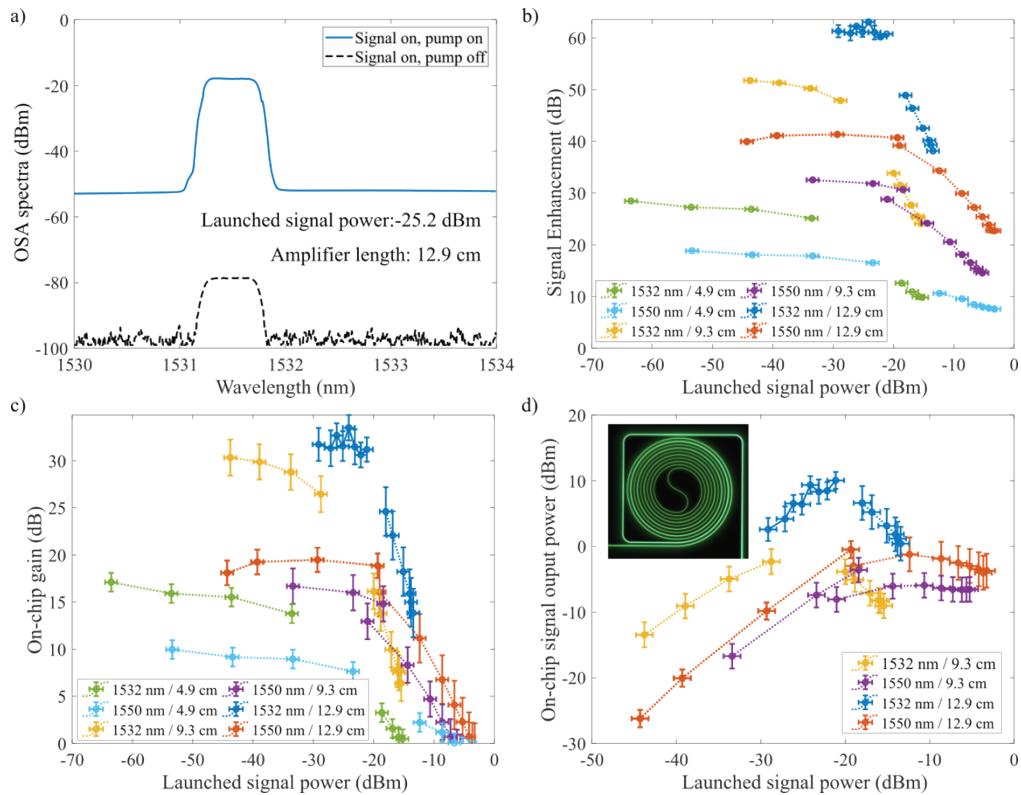


Fig. 4. a) OSA spectra demonstrating a signal enhancement of ~ 63 dB. b) Signal enhancement, c) On-chip net gain, and d) On-chip signal output power for varying waveguide lengths at 1532 and 1550 nm for low and high launched signal powers with inset image of the inverted 12.9 cm amplifier during measurement.

where the system losses, α_{sys} , were measured to be -1.65 dB, and the losses of the OSA, α_{OSA} , were characterized as -4.5 dB. Using measured data for different levels of incident input signal, an average coupling loss of -25 dB per facet was obtained for a signal wavelength of 1532 nm (~ -15.5 dB at 1550 nm), where at the pump this value is much lower, namely -7.5 dB of coupling losses. This signal coupling loss is much higher than the loss estimated by design (i.e., -4 dB/facet for a taper tip width of 303 nm, as shown in Fig. 1 (c)). This can partially be accounted for by the artifact observed on the cladding of the input tapers (Fig. 1 (b)), produced during the non-conformal PECVD deposition process, and is anticipated to be exacerbated by the inner sidewall roughness of this void. The additional wavelength dependency is anticipated to be caused by absorption along the nanotaper length, which in this study has been lumped together with the facet losses caused by mode mismatch and the void. Optimization of the edge couplers is currently ongoing, on the way towards achieving fiber-to-fiber external net gain.

The on-chip output power was calculated from the measured power at the OSA, P_{OSA} , and the different loss contributions of the system. A peak on-chip power of 10.2 ± 1.3 dBm was obtained for a launched signal of -25.2 dBm at 1532 nm in a 12.9 cm amplifier, which corresponds to ~ 10 mW of on-chip power and approximately 15% pump power conversion efficiency. The on-chip power for different levels of launched input signal and different amplifier lengths are shown in Fig. 4 (d) for both 1532 as well as 1550 nm of signal wavelength.

5. Discussion

When comparing to other state-of-the-art demonstrations of on-chip rare-earth ion doped optical waveguide amplifiers many considerations need to be made. Various aspects such as the fabrication method and material platform can affect the scalability or integration capability of these devices. While atomic layer deposition has shown very high gain per unit length when in combination with Si_3N_4 waveguides in slot geometry [24], it is a slow deposition method not easily applicable for the deposition of the thick layers required for optical amplifiers (i.e., hundreds of nanometers). On the other hand, ion implantation has been shown to yield very high quality doped layers [15]. Again, implantation of such high doping levels is difficult to implement in a scalable way and requires very high temperature annealing for the recovery of the waveguide performance, damaged after the ion bombardment. Table 1 lists a variety of recent results for optical amplifiers ranging from erbium doped waveguides formed through sputtering, ALD and ion-implantation. EDFA performance is included as reference.

Table 1. Comparison to state-of-the-art small signal gain peak values

Material	Fabrication Method	On-chip net gain (dB)	On-chip signal power (dBm)	Gain / unit length (dB/cm)	Erbium concentration ($\times 10^{20}$ ions/cm ³)	Ref
$\text{Al}_2\text{O}_3:\text{Er}^{3+}$	Sputtering	33.5	13.2	3.5	3.9	This work
$\text{Al}_2\text{O}_3:\text{Er}^{3+}$	Sputtering	17.0	14.7	1.5	3.9	[38]
$\text{Al}_2\text{O}_3:\text{Er}^{3+}$	Sputtering	20.0	4.0	1.5	1.9	[12]
$\text{Al}_2\text{O}_3:\text{Er}^{3+}$	Sputtering	9.3	-30.0	2.0	1.2	[11]
$\text{Al}_2\text{O}_3:\text{Er}^{3+}:\text{Yb}^{3+}$	Sputtering	4.3	-8.5	1.4	1.5	[18]
$\text{TeO}_2:\text{Er}^{3+}$	Sputtering	14.0	13.0	2.8	2.2	[7]
$\text{Si}_3\text{N}_4 / \text{TeO}_2:\text{Er}^{3+}$	Sputtering	5.0	<-1.0	1.3	2.5	[8]
$\text{Si}_3\text{N}_4 / \text{Al}_2\text{O}_3:\text{Er}^{3+}$	Sputtering	7.5	13.0	0.8	2.5	[34]
$\text{Si}_3\text{N}_4 / \text{Al}_2\text{O}_3:\text{Er}^{3+}$	Sputtering	18.1	2.7	1.3	1.7	[29]
$\text{Si}_3\text{N}_4:\text{Er}^{3+}$	Ion implantation	30.0	21.6	1.4	3.3	[15]
$\text{Si}_3\text{N}_4 / \text{Al}_2\text{O}_3:\text{Er}^{3+}$	ALD	0.4	-20.0	20.0	20	[24]
Er-doped fiber	N/A	> 30.0	>20.0	N/A	N/A	Thorlabs EDFA100S

When comparing to other results particularly in $\text{Al}_2\text{O}_3:\text{Er}^{3+}$ a major difference between the work demonstrated here and the others is the use of annealing in a polycrystalline host material. This contrasts to other works in amorphous hosts, which are incapable of being annealed and where the erbium ions encounter a different local environment. This result therefore marks a major step towards realizing high gain for $\text{Al}_2\text{O}_3:\text{Er}^{3+}$ waveguide amplifiers fabricated via reactive sputtering. Unfortunately, the edge couplers in this work exhibited high coupling losses, limiting the amount of on-chip power obtained and ultimately the achievement of fiber-to-fiber net gain. Future work will be geared towards optimizing the coupling losses and investigating a variety of dopant concentrations and increased waveguide lengths. Additionally, future studies on the quenching [39], spectroscopy, and polycrystallinity of the material to enable modelling and optimization of the amplifier design and ideal fabrication conditions can aid in the discovery of parameters for achieving even higher gain and saturation power.

6. Conclusion

Reactive magnetron sputtering has been utilized to fabricate $\text{Al}_2\text{O}_3:\text{Er}^{3+}$ waveguides which demonstrate record high gain at 1532 nm of 33.5 dB, with ~10 mW (~10 dBm) of on-chip power

for a 12.9 cm amplifier. Spirals of different lengths were measured for varying pump and signal powers, demonstrating peak on-chip gain per unit length of 3.5 dB/cm at 1532 nm in a 4.9 cm amplifier. The results have promise of being improved by further reduction of the background and coupling losses by further optimizing the fabrication process.

Funding. Horizon 2020 Framework Programme (101017136).

Acknowledgments. The authors wish to acknowledge Quentin Coulaud for the theoretical development of the 1480 nm bi-directional pumping scheme for the waveguide amplifiers, and Frans Segerink for performing focused ion-beam milling in order to inspect waveguide facets. The authors also wish to acknowledge the support from the Centro de Microanálisis de Materiales (CMAM)—Universidad Autónoma de Madrid, for the beam time access under the proposal code STD035/21, and its technical staff for their contribution to the operation of the accelerator used for RBS. The authors acknowledge funding from the European Union’s Horizon 2020 research and innovation programme under Grant Agreement No 101017136.

Disclosures. The authors declare no conflicts of interest.

Data availability. Data underlying the results presented in this paper are not publicly available at this time but may be obtained from the authors upon reasonable request.

References

1. T. Chrysostomidis, J. Mu, I. Roumpos, *et al.*, “8×40 Gbps WDM Amplification in a Monolithically Integrated Al₂O₃:Er³⁺-Si₃N₄ Waveguide Amplifier,” *IEEE Photonics Technol. Lett.* **33**(21), 1177–1180 (2021).
2. J. Notaros, N. Li, C. V. Poulton, *et al.*, “CMOS-Compatible Optical Phased Array Powered by a Monolithically-Integrated Erbium Laser,” *J. Lightwave Technol.* **37**(24), 5982–5987 (2019).
3. E. H. Bernhardt, K. O. van der Werf, A. J. F. Hollink, *et al.*, “Intra-laser-cavity microparticle sensing with a dual-wavelength distributed-feedback laser,” *Laser Photonics Rev.* **7**(4), 589–598 (2013).
4. L. He, Ş. K. Özdemir, J. Zhu, *et al.*, “Detecting single viruses and nanoparticles using whispering gallery microlasers,” *Nat. Nanotechnol.* **6**(7), 428–432 (2011).
5. N. Singh, J. Lorenzen, M. Sinobad, *et al.*, “Watt-class CMOS-compatible power amplifier,” *arXiv*, arXiv:2306.12940 (2023).
6. A. Aghajani, G. S. Murugan, N. P. Sessions, *et al.*, “Waveguide lasers in ytterbium-doped tantalum pentoxide on silicon,” *Opt. Lett.* **40**(11), 2549–2552 (2015).
7. K. Vu and S. Madden, “Tellurium dioxide Erbium doped planar rib waveguide amplifiers with net gain and 2.8 dB/cm internal gain,” *Opt. Express* **18**(18), 19192–19200 (2010).
8. H. C. Frankis, H. M. Mbonde, D. B. Bonneville, *et al.*, “Erbium-doped TeO₂-coated Si₃N₄ waveguide amplifiers with 5 dB net gain,” *Photonics Res.* **8**(2), 127–134 (2020).
9. K. M. Kiani, H. C. Frankis, C. M. Naraine, *et al.*, “Lasing in a hybrid rare-earth silicon microdisk,” *Laser Photonics Rev.* **16**(1), 2100348 (2022).
10. K. Worhoff, J. D. Bradley, F. Ay, *et al.*, “Reliable low-cost fabrication of low-loss Al₂O₃:Er³⁺ waveguides with 5.4-dB optical gain,” *IEEE J. Quantum Electron.* **25**(5), 454–461 (2009).
11. J. D. B. Bradley, L. Agazzi, D. Geskus, *et al.*, “Gain bandwidth of 80 nm and 2 dB/cm peak gain in Al₂O₃:Er³⁺ optical amplifiers on silicon,” *J. Opt. Soc. Am. B* **27**(2), 187–196 (2010).
12. S. A. Vázquez-Córdova, M. Dijkstra, E. H. Bernhardt, *et al.*, “Erbium-doped spiral amplifiers with 20 dB of net gain on silicon,” *Opt. Express* **22**(21), 25993 (2014).
13. J. Zhou, Y. Liang, Z. Liu, *et al.*, “On-chip integrated waveguide amplifiers on Erbium doped thin film lithium niobate on insulator,” *Laser Photonics Rev.* **15**(8), 2100030 (2021).
14. Z. Zhang, S. Li, R. Gao, *et al.*, “Erbium-ytterbium codoped thin-film lithium niobate integrated waveguide amplifier with a 27 dB internal net gain,” *Opt. Lett.* **48**(16), 4344–4347 (2023).
15. Y. Liu, Z. Qiu, X. Ji, *et al.*, “A photonic integrated circuit-based erbium-doped amplifier,” *Science* **376**(6599), 1309–1313 (2022).
16. J. D. B. Bradley and M. Pollnau, “Erbium-doped integrated waveguide amplifiers and lasers,” *Laser Photonics Rev.* **5**(3), 368–403 (2011).
17. N. Singh, J. Lorenzen, M. Sinobad, *et al.*, “Silicon photonics-based high-energy passively Q-switched laser,” *Nat. Photonics* (2024).
18. D. B. Bonneville, H. C. Frankis, R. Wang, *et al.*, “Erbium-ytterbium co-doped aluminium oxide waveguide amplifiers fabricated by reactive co-sputtering and wet chemical etching,” *Opt. Express* **28**(20), 30130 (2020).
19. J. Yang, K. van Dalfsen, K. Wörhoff, *et al.*, “High-gain Al₂O₃:Nd³⁺ channel waveguide amplifiers at 880 nm, 1060 nm, and 1330 nm,” *Appl. Phys. B* **101**(1–2), 119–127 (2010).
20. K. Van Gasse, R. Wang, and G. Roelkens, “27 dB gain III–V-on-silicon semiconductor optical amplifier with > 17 dBm output power,” *Opt. Express* **27**(1), 293 (2019).
21. W. Q. Wei, A. He, B. Yang, *et al.*, “Monolithic integration of embedded III-V lasers on SOL,” *Light: Sci. Appl.* **12**(1), 84 (2023).

22. O. de Beeck, B. Haq, L. Elsinger, *et al.*, "Heterogeneous III-V on silicon nitride amplifiers and lasers via microtransfer printing," *Optica* **7**(5), 386–393 (2020).
23. Y. Lin, C. Browning, R. B. Timens, *et al.*, "Characterization of hybrid InP-triplex photonic integrated tunable lasers based on silicon nitride ($\text{Si}_3\text{N}_4/\text{SiO}_2$) microring resonators for optical coherent system," *IEEE Photonics J.* **10**(3), 1400108 (2018).
24. J. Rönn, W. Zhang, A. Autere, *et al.*, "Ultra-high on-chip optical gain in erbium-based hybrid slot waveguides," *Nat. Commun.* **10**(1), 432 (2019).
25. W. A. P. M. Hendriks, L. Chang, C. I. Van Emmerik, *et al.*, "Rare-earth ion doped Al_2O_3 for active integrated photonics," *Adv. Phys.: X* **6**(1), 1 (2021).
26. D. Che, S. Grillanda, Y. Liu, *et al.*, "First Demonstration of Erbium-Doped Waveguide Amplifier Enabled Multi-Tb/s (16×1.6 T) Coherent Transmission," in *Proceedings of Optical Fiber Communication Conference*, (2023).
27. C. He, Y. Wang, C. Waldfried, *et al.*, "Ultra-high Q alumina optical microresonators in the UV and blue bands," *Opt. Express* **31**(21), 33923 (2023).
28. C. A. A. Franken, W. A. P. M. Hendriks, L. V. Winkler, *et al.*, "Hybrid integrated near UV lasers using the deep-UV Al_2O_3 platform," *arXiv*, arXiv:2302.11492 (2023).
29. J. Mu, M. Dijkstra, J. Kortarik, *et al.*, "High-gain waveguide amplifiers in Si_3N_4 technology via double-layer monolithic integration," *Photonics Res.* **10**(8), 1634–1641 (2020).
30. M. A. Gaafar, M. Ludwig, K. Wang, *et al.*, "Femtosecond pulse amplification on a chip," *arXiv*, arXiv:2311.04758 (2023).
31. Z. Su, N. Li, H. C. Frankis, *et al.*, "High-Q-factor Al_2O_3 micro-trench cavities integrated with silicon nitride waveguides on silicon," *Opt. Express* **26**(9), 11161 (2018).
32. L. Agazzi, K. Wörhoff, A. Kahn, *et al.*, "Spectroscopy of upper energy levels in an Er^{3+} -doped amorphous oxide," *J. Opt. Soc. Am. B* **30**(3), 663 (2013).
33. W. A. P. M. Hendriks, M. Dijkstra, I. Hegeman, *et al.*, "Poly-crystalline low-loss aluminium oxide waveguides," in *Proceedings of SPIE - The International Society for Optical Engineering* **11689**, (2021).
34. C. E. Osornio-Martinez, D. B. Bonneville, M. Dijkstra, *et al.*, "Optical gain via multi-layer monolithic integration of Si_3N_4 with $\text{Al}_2\text{O}_3:\text{Er}^{3+}$ waveguide amplifiers," in *Proceedings of European Conference on Integrated Photonics*, (2023).
35. C. I. Emmerik, W. A. P. M. Hendriks, M. M. Stok, *et al.*, "Relative oxidation state of the target as guide line for depositing optical quality RF reactive magnetron sputtered Al_2O_3 layers," *Opt. Mater. Express* **10**(6), 1 (2020).
36. A. Redondo-Cubero, M. J. G. Borge, N. Gordillo, *et al.*, "Current status and future developments of the ion beam facility at the centre of micro-analysis of materials in Madrid," *Eur. Phys. J. Plus* **136**(2), 175 (2021).
37. E. S. Magden, "Rare-earth doped aluminium oxide lasers for silicon photonics," (Ph.D. Thesis, Massachusetts Institute of Technology, 2014).
38. D. B. Bonneville, C. E. Osornio-Martinez, M. Dijkstra, *et al.*, "Material optimization via optical and spectroscopic parameters of $\text{Al}_2\text{O}_3:\text{Er}^{3+}$ for the development of amplifiers and lasers," in *Proceedings of IEEE Benelux*, (2022).
39. L. Agazzi, Spectroscopic Excitation and Quenching Processes in Rare-Earth-Ion-Doped Al_2O_3 and their Impact on Amplifier and Laser Performance, (Ph.D. Thesis, University of Twente, 2012).